JOINT EUROPEAN TORUS

JET–P(95)64

Many Authors

JET Papers presented to the 6th European Fusion Theory Conference (Utrecht, The Netherlands, 2-4 October 1995)

JET Papers presented to the 6th European Fusion Theory Conference (Utrecht, The Netherlands, 2-4 October 1995)

Many Authors

JET-Joint Undertaking, Culham Science Centre, OX14 3EA, Abingdon, UK

Preprint of Papers to be submitted for publication in
the Proceedings of the 6th European Fusion Theory Conference
(Utrecht, The Netherlands, 2-4 October 1995)

November 1995

JET Papers and Posters presented to the
6th European Fusion Theory Conference
(Utrecht, The Netherlands, 2-4 October 1995)

Contents

Influence of X-point on Edge Plasma MHD Stability

W Kerner, O Pogutse, R A M Van der Linden.
JET Joint Undertaking, Abingdon, Oxfordshire, OX14 3EA, UK.

INTRODUCTION

1. The tokamak edge plasma includes a part of the core plasma and a part of the scrape-off-layer about a few Larmor radii inside and outside the separatrix. These parts have quite different topology with closed and open magnetic field lines (where the plasma interacts with the end plates). Due to MHD activities these two areas can interact. Therefore, this edge plasma plays a critical role in the behaviour of the entire plasma and in phenomena such as L-H transition and ELM's.

2. Theoretical analysis of the edge plasma leads to the following picture of the discharge evolution:

   i) In the initial phase the edge plasma is cold and exhibits low conductivity, which leads to dissipative (resistive interchange - and drift - type) instabilities at the plasma edge causing strong turbulent transport. This turbulence can be transferred into the plasma centre by means of a pumping mechanism or by an extended radial mode structure. This phase constitutes the **L-regime**.

   ii) With increasing edge temperature the dissipative instabilities in the edge plasma become weaker, the transport coefficients decrease and the gradients at the boundary increase. The profile of the pressure (along with temperature and density) becomes increasingly more step-like. For such steep gradients the Larmor radius stabilisation and the shear flow stabilisation take place, turbulence is suppressed and the **H-mode** is set up.

3. The development of a step-like pressure profile in the H-mode will lead to unstable MHD surface modes, which may explain the essential properties of the giant ELM phenomenon.

   In the edge physics the structure of the separatrix and, in particular, the region around the X-point play an essential role.

4. The results of the ideal interchange instability analysis in the relevant X-point geometry are presented.

   The stability analysis is performed separately in the region inside and outside the separatrix. The magnetic well has a strong stabilising effect for the plasma inside the separatrix (second stability domain) - but outside the separatrix this effect is absent. Consequently, the outer plasma part can be more unstable, but the free energy source is small there.

   - MHD instabilities in the open field line plasma can trigger the release of the free energy stored inside the separatrix.

   - Stability analysis outside the separatrix is relevant for SOL problems.

JET discharge

↓

Equilibrium reconstruction : EFIT

↓

Flux coordinate system ρ, ω, φ : GRID2D (Simonini et al.)

↓

Ballooning stability analysis ($nq >> 1$)

Coordinate System in SOL:

The magnetic field line geometry is described by the orthogonal coordinates ρ, ω, φ:

$$ds^2 = h_\rho^2 d\rho^2 + h_\omega^2 d\omega^2 + R^2 d\varphi^2$$

Eikonal representation for perturbed electrostatic potential (J.Connor, R.J. Hastie and B. Taylor, Proc. R. Soc. Lond. A.365, 1, 1979):

$$\phi(t,\rho,\omega,\varphi) = \tilde{\phi}(\rho,\omega)\cdot \exp(\gamma t + in\int_{\omega 0}^{\omega} q(\rho,\omega')d\omega' - in\varphi)$$

leads to:

$$B_o\left(\frac{B_\omega}{h_\omega B_0}\frac{\partial}{\partial\omega}\right)\frac{1}{B_o}\left(\frac{nq}{h_\omega}\right)^2(1+\zeta^2)\left(\frac{B_\omega}{h_\omega B_0}\frac{\partial}{\partial\omega}\right)\tilde{\phi} - \gamma^2 C_A^{-2}\left(\frac{nq}{h_\omega}\right)^2(1+\zeta^2)\tilde{\phi}$$
$$- \frac{4\pi}{RB_0}\left(\frac{nq}{h_\omega}\right)^2\frac{1}{h_\rho}\left(\frac{1}{h_\rho}\frac{\partial}{\partial\rho}\frac{R}{B_0} - \zeta\frac{1}{h_\omega}\frac{\partial}{\partial\omega}\frac{R}{B_0}\right)\frac{dP_0}{d\rho}\tilde{\phi} = 0$$

Safety factor: $$q = q(\rho,\omega) = \frac{B_0 h_\omega}{B_\omega R},$$

shear: $$\zeta = \zeta(\rho,\omega,\omega 0) = (h_\omega / h_\rho)\left(\frac{\partial}{\partial\rho}\int_{\omega 0}^{\omega} q d\omega\right)/q.$$

For an analytic model we use magnetic field components:

$$B_\omega = B_\omega(\rho,\omega) = B_\omega(\rho,\pi)\cdot\frac{h_\omega(\pi)R(\pi)}{h_\omega(\rho,\omega)R(\rho,\omega)},$$

$$B_0 = B_0(\rho,\omega) = B_0(\pi)\cdot\frac{R(\pi)}{R(\rho,\omega)},$$

and choose simpler coordinates derived in a straight cylinder with $h_\rho^2 = h_\omega^2 = h^2$

$$h^2 = \frac{y_0^2}{2^{5/2}}\cdot\frac{1}{[1-\cos(\omega)+\rho^2/2]^{1/2}};$$

y_o is the distance of the current wire from the X-point. We introduce

$$R = R(\rho,\omega) = R_0 + x(\rho,\omega),$$

and obtain

$$x(\rho,\omega) = (+/-)y_0 / \sqrt{2} \cdot [-1+\cos(\omega)+\rho+\sqrt{2}(1-\cos(\omega)+\rho^2/2)^{1/2}]^{1/2} .$$

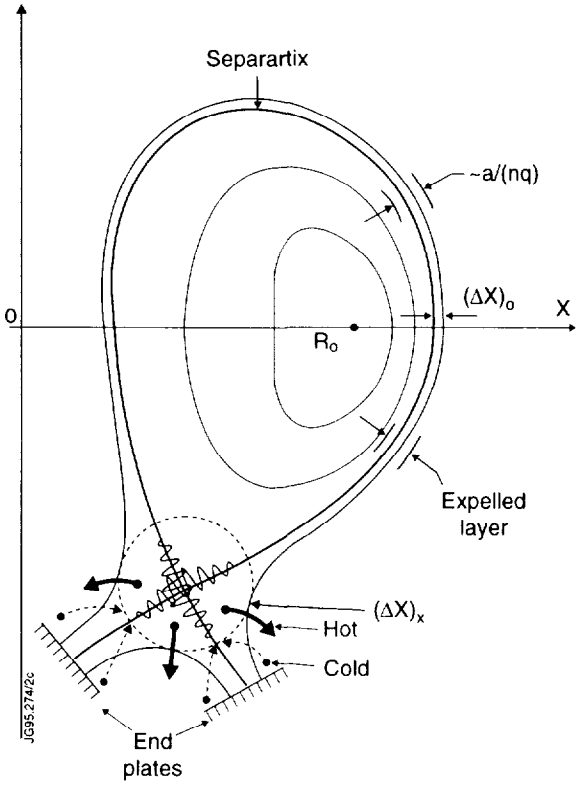

Fig.1: JET divertor plasma.

NUMERICAL RESULTS

- Influence of X-point

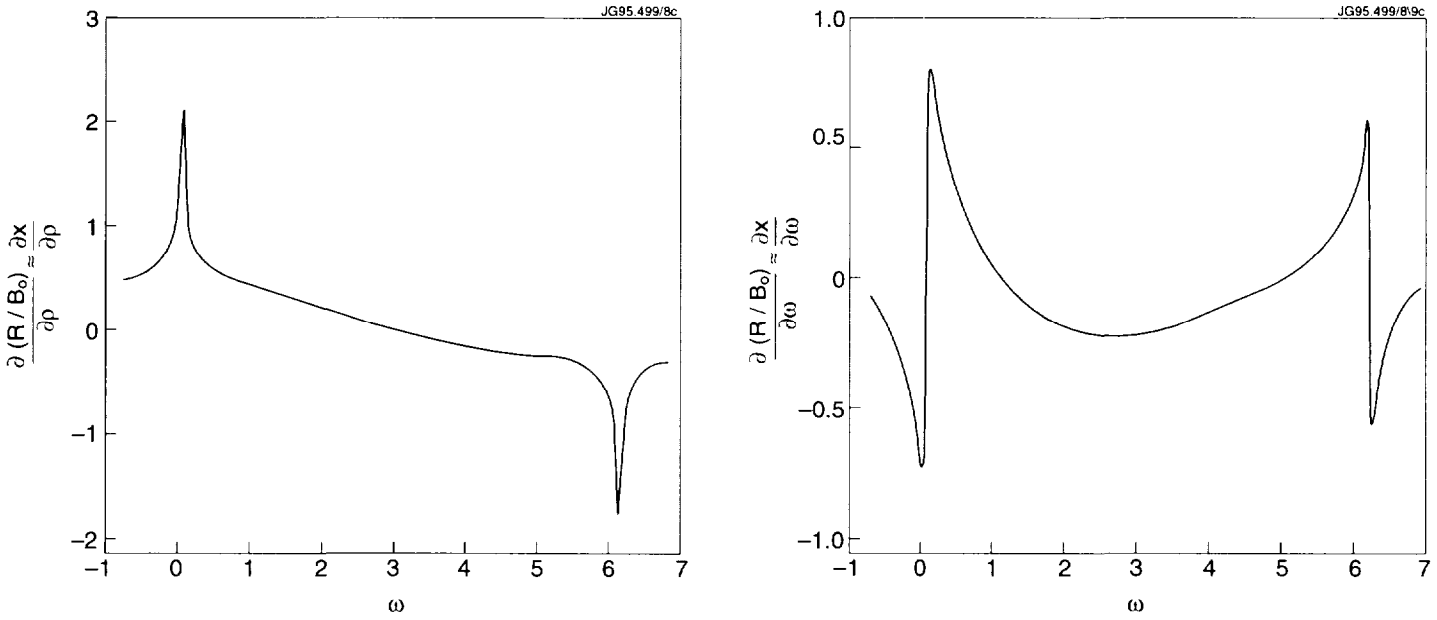

Fig.2: Dependence of equilibrium on ρ, ω.

- Strong variation near X-point

$$\tilde{\beta} = \frac{4\pi p_o}{B_o^2} \frac{1}{p_o} \frac{dp_o}{d\rho} \quad ; \quad S_o = \frac{1}{q(\rho,\pi)} \frac{\partial}{\partial \rho} \; q(\rho,\omega)$$

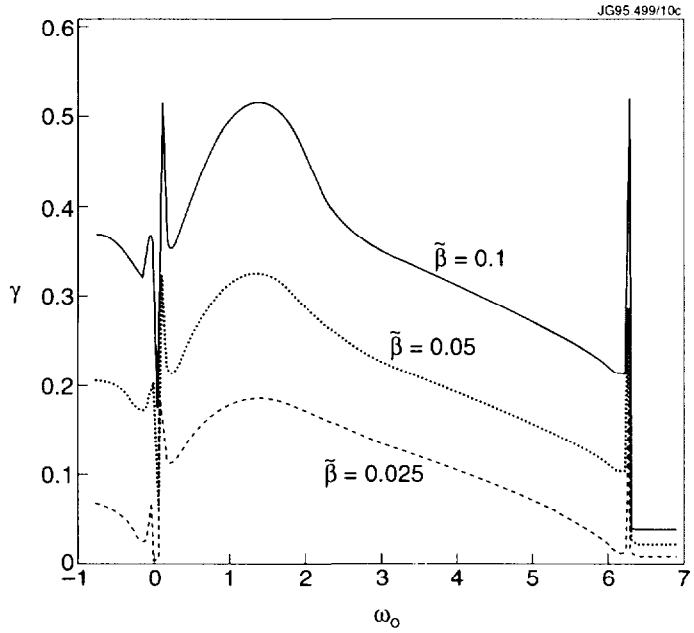

Fig.3a: Growth rates

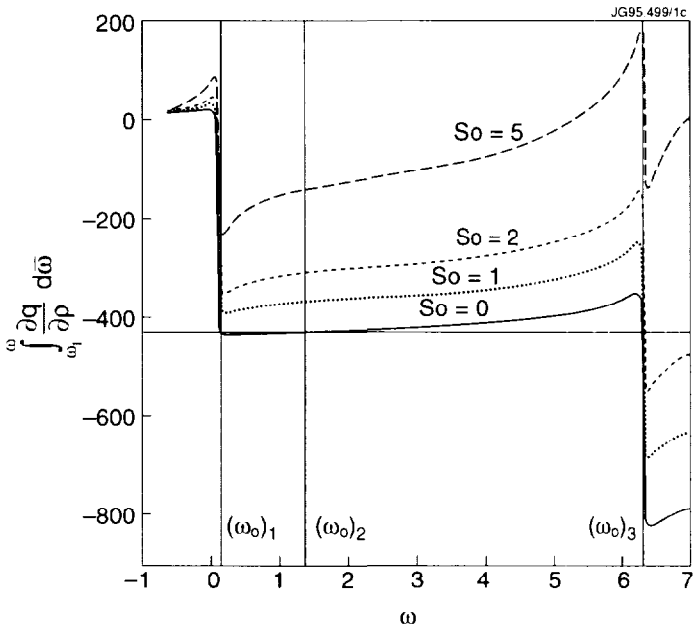

Fig.3b: Integrated Shear

- Non-monotonic behaviour of $\frac{\partial q}{\partial \rho}$ in dependence on ω.
- Similar results for a JET experimental configuration based on an EFIT equilibrium reconstruction applying GRID2D.

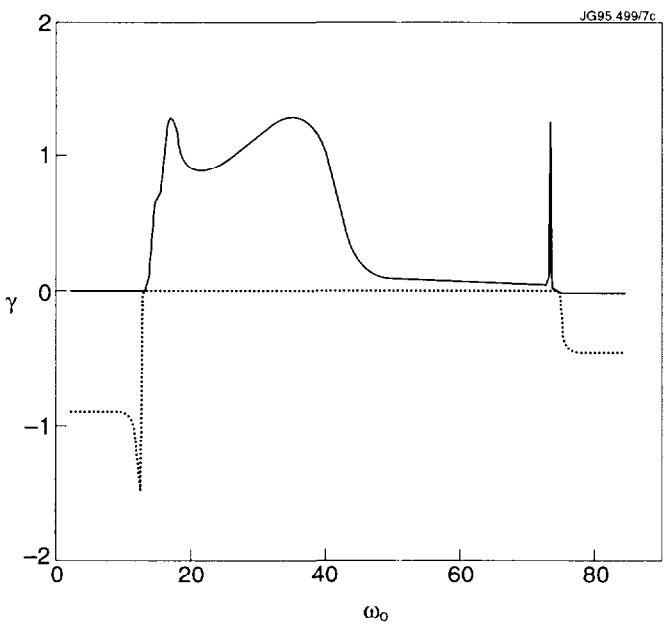

Fig.4a: Growth rates

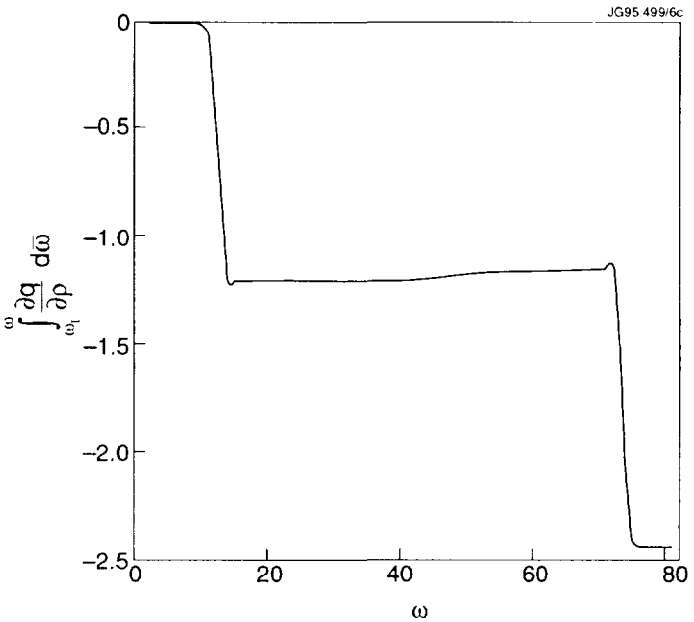

Fig.4b: Integrated Shear

- Critical $\tilde{\beta}$

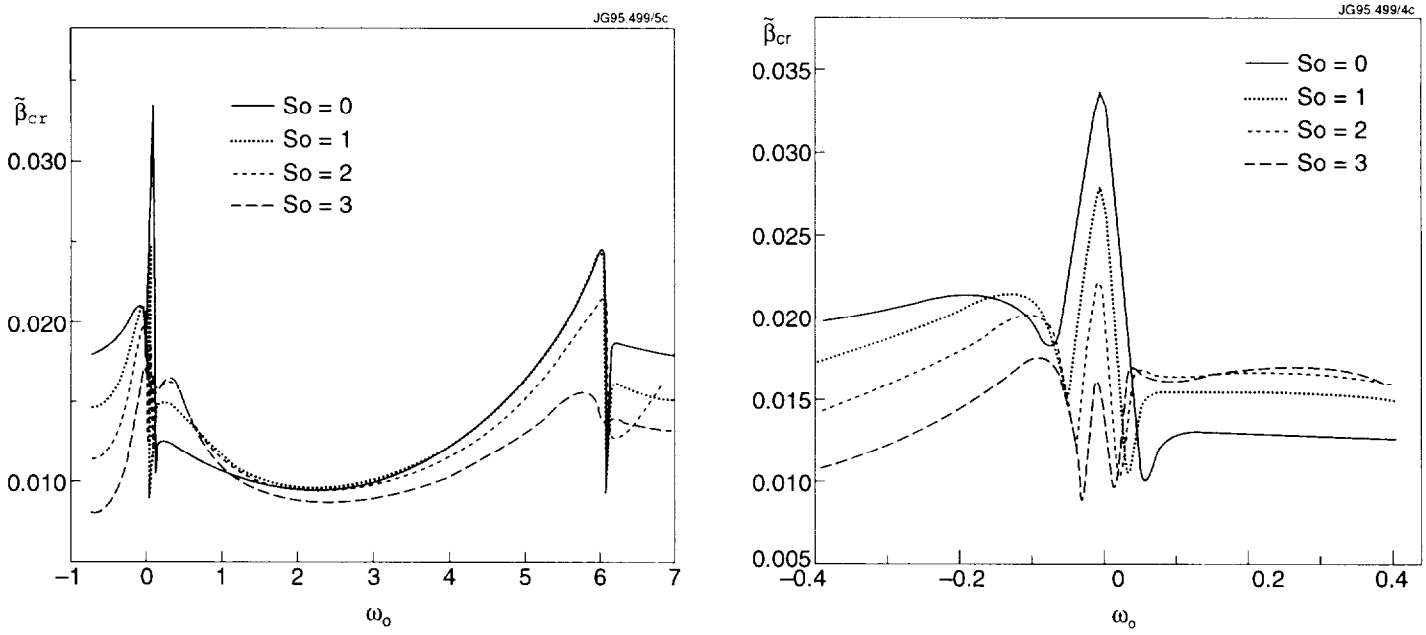

Fig.5: Dependence of critical $\tilde{\beta}$ on shear.

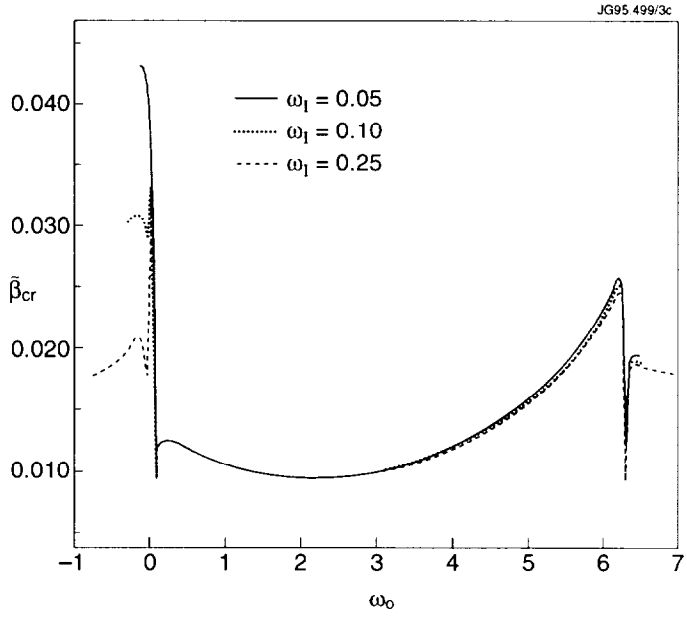

Fig.6: Dependence on X-point height

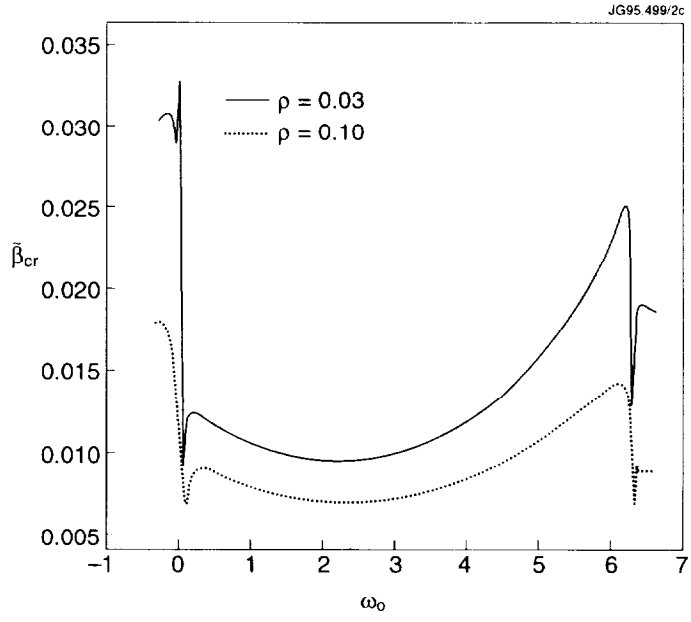

Fig.7: Dependence on radial distance

- Distance in ω between the X-point and the target plates (line-tying) is not important. Boundary conditions at target plates are not essential.

ANALYTIC APPROXIMATION

After suitable normalisation the ballooning equation near the X-point is brought into Schrödinger-type form in the new variable $t = \omega/\rho$.

For the new function u(t):

$$\phi(t) = \frac{1}{\sqrt{1+t^2}} u(t)$$

We find the equation:

$$u''_{tt} - V(t)u = 0$$

and $V(t) = V_s(t) + \hat{\beta}.V_d(t)$; where $\hat{\beta} = \left(2^{7/2}\frac{R(\pi)}{y_0}\rho^{1/2}q^2(\pi)\right)\tilde{\beta}$;

$$V_s(t) = \left(\frac{\Gamma^2}{(1+t^2)} + \frac{1}{(1+t^2)^2}\right); \quad V_d(t) = -\left(\frac{\left[1+(1+t^2)^{1/2}\right]^{1/2}}{(1+t^2)^{3/2}}\right),$$

here $\Gamma^2 = \frac{\gamma^2 q(\rho,\pi)^2 h(\pi)^2}{C_A^2}$ is the normalised growth rate.

This equation can be derived from the variational form:

$$E = \frac{1}{2}\int_{-\infty}^{\infty}\left[(u'_t)^2 + V(t)\cdot u^2\right]dt$$

The variational form is very convenient to estimate the growth rate and the marginal stability criterion. By choosing $u(t) = c_1$, where c_1 is constant, and varying c_1 we find the condition $\int_{-\infty}^{\infty} V(t)\,dt = 0$. The threshold beta for $\omega_o = 0$, $S_o = 0$ is given by:

$$\hat{\beta}_{cr} = -\frac{\int_{-\infty}^{\infty} V_s(t)dt}{\int_{-\infty}^{\infty} V_d(t)dt} = \frac{\int_{-\infty}^{\infty}(1+t^2)^{-2}dt}{\int_{-\infty}^{\infty}\left[1+(1+t^2)^{1/2}\right]^{1/2}(1+t^2)^{-3/2}dt} = 0.5,$$

which differs about a factor of two from the numerical result

$$\left(\tilde{\beta}_{cr}\right)_{an} \approx 0.06 \approx 2 \times \left(\tilde{\beta}_{cr}\right)_{num}$$

Stability criterion expressed in mid-plane plasma parameters

$$\frac{q(\pi)^2 4\pi P_0}{B_0(\pi)^2} > \frac{1}{2^{3/2}} \frac{y_0}{R(\pi)} \left(\frac{(\Delta x)_0}{y_0} \right)^{1/2} \propto \frac{b}{R_0} \left(\frac{(\Delta x)_0}{b} \right)^{1/2} \propto \frac{(\Delta x)_x}{R_o}$$

- Stability analysis is applicable inside the separatrix, $\rho < 0$. Even without the magnetic well taken fully into account $\hat{\beta}_{cr}$ is larger than in SOL.

- Open field line plasma more relevant for interchange instabilities.

CONCLUSIONS

- Ballooning stability analysis performed in plasma near X-point.

- X-point strongly screens the influence of boundary conditions for the perturbations localised close to the separatrix.

- Critical $\tilde{\beta}$ is found to be quite small in agreement with typical SOL plasmas $\left(\beta \lesssim 10^{-4}\right)$.

- Influence of magnetic well (second stability domain) is effective inside the separatrix but not outside.

- Physical perturbations, e.g. δB_ρ, v_ρ, are localised near the X-point.

- SOL MHD instability can be precursor for giant ELM's.

  Influx of cold plasma causes "defreezing" of magnetic field lines thereby releasing the free energy stored near the separatrix in H-mode plasmas.

Comparison Between JET Profile Data and the Predictions of a Reactive Drift Wave Model for Anomalous Transport

P. Strand, H. Nordman, M. Fröjdh, J.Weiland
Institute for Electromagnetic Field Theory
Chalmers University of Technology, Göteborg, SWEDEN
EUROATOM-NFR Association

J.P. Christiansen
JET Joint Undertaking
Culham, Abingdon, Oxon OX14 3EA, UK

Abstract

The predictions of a reactive drift wave model for anomalous transport in tokamaks, [Nucl. Fusion **30**,983, 1990], is compared with JET profile data. Density and temperature profiles are self-consistently calculated with a predictive simulation code and compared with the experimental profiles.

The model is intended for the good confinement region where the results are in good agreement with experiments. For the range of discharges studied relative errors $\leq 20\%$ were obtained.

Experimental profiles have been obtained from the interpretative code TRANSP.

Work performed under JET Task Agreement NFR/TA4

Transport Coefficients

The transport model employed in this study [1] is a higher moment fluid model [2]. In this model a combination of the toroidal branch of the **I**on **T**emperature **G**radient mode (ITG) and the **C**ollisionless **T**rapped **E**lectron mode (CTE) drives the transport. Net transport across the magnetic field-lines is obtained by quasi-linear theory and a saturation level estimate. The effective transport coefficients take the form:

$$\chi_i^{eff} = \frac{1}{\eta_i}\left\{\eta_i - \frac{2}{3} - (1-f_t)\frac{10}{9\tau}\epsilon_n - \frac{2}{3}f_t\Delta_i\right\}\frac{\gamma^3/k_x^2}{\left(\omega_r - \frac{5}{3}\omega_{D_i}\right)^2 + \gamma^2}$$

$$\chi_e^{eff} = f_t\frac{1}{\eta_e}\left\{\eta_e - \frac{2}{3} - \frac{2}{3}\Delta_e\right\}\frac{\gamma^3/k_x^2}{\left(\omega_r - \frac{5}{3}\omega_{D_e}\right)^2 + \gamma^2}$$

$$D^{eff} = f_t\Delta_n\frac{\gamma^3/k_x^2}{\omega_{\star e}^2}$$

Here the Δ_j are phase shifts due to the trapped electron density perturbation and are quite complicated functions of $\omega, \epsilon_n, \eta_i, \eta_e$ and τ. The eigenvalues, $\omega = \omega_r + i\gamma$, can be obtained from a dispersion relation, and the transport coefficients are summed over the unstable modes. The space-scale of the turbulence is fixed by choosing $k^2\rho^2 = 0.1$ which corresponds to the scale of the most unstable mode.

$$\frac{\delta n_i}{n} = f_t\frac{\delta n_{et}}{n_{et}} + (1-f_t)\frac{e\Phi}{T_e}$$

where f_t is the fraction of trapped electrons and the density responses for the ions (n_i) and the trapped electrons (n_{et}) are written as

$$\frac{\delta n_j}{n} = \omega_{\star e}\frac{\omega(1-\epsilon_n) - \left(\frac{7}{3} - \eta_j - \frac{5}{3}\epsilon_n\right)\omega_{D_j} + \delta_{j,i}FLR}{\omega^2 - \frac{10}{3}\omega\omega_{D_j} + \frac{5}{3}\omega_{D_j}^2}\frac{e\Phi}{T_e}$$

In the above expressions the following notation is used

$$\epsilon_n = \frac{\omega_D}{\omega_\star} = 2\frac{\mathcal{L}_n}{\mathcal{L}_B}, \qquad \eta_j = \frac{\mathcal{L}_n}{\mathcal{L}_{T_j}}, \qquad \tau = \frac{T_e}{T_i}$$

Predictive Transport Simulations

The temporal evolution of $\vec{u} = (p_i, p_e, n)$ is followed self-consistently together with the transport coefficients under the assumption of quasi-neutrality. For a prescribed equilibrium, assuming $\frac{\partial V'}{\partial t} = 0$, the transport equations are:

$$\frac{3}{2}\frac{\partial p_j}{\partial t} + \frac{1}{V'}\frac{\partial}{\partial \rho}\left\{V'\left[< \vec{q}_j \cdot \nabla\rho > + \frac{3}{2}T_j\Gamma_j\right]\right\} =< S_j >, \quad j = i, e$$

$$\frac{\partial n}{\partial t} + \frac{1}{V'}\frac{\partial}{\partial \rho}\{V'\Gamma_j\} =< S_n >$$

The effects of a changing equilibrium configuration are then included by the introduction of adiabatic constraints [5] requiring the quantities nV' and $p_j V'^{5/3}$ to be conserved whenever V' changes.

Defining the radial fluxes in terms of the effective transport coefficients described previously provides a natural matrix formulation of the transport equations. Within this formulation $< \vec{q}_i \cdot \nabla\rho >$ will be proportional to $T_i, \nabla T_i, \nabla T_e$ and ∇n providing diagonal and off-diagonal elements in the transport matrix.

Since the transport coefficients of the ITG/CTE model described here tend to zero towards the axis, additional transport is needed in this region. For this purpose constant transport coefficients $\chi_i = 2\chi_e = 4D = 0.5$ were added to the corresponding diagonal elements in the transport matrix out to a radius $\rho = 0.3$.

Boundary conditions:

$$\begin{cases} \left.\dfrac{\partial u_j}{\partial \rho}\right|_{\rho=0} = 0 \\ \\ u_j|_{\rho=a} = f_j(t) \end{cases} \quad j = 1, 2, 3$$

The boundary values for the profiles $f_j(t)$ are updated from JET profile databases [6, 7] at each timestep, together with source terms and geometrical quantities.

The resulting system of coupled non-linear PDEs is solved with standard finite differences (FD) techniques using a predictor-corrector approach for the nonlinearities.

L-mode shots

The code has been run on the following set of L-mode discharges

Shot no: time	I_p (MA)	B_T T)	$n_e(0)$ $10^{19}(m^{-3})$	$T_e(0)$ (keV)	$T_i(0)$ (keV)	P_{ICRH} (MW)	P_{NBI} (MW)
15596 $44.0 < t < 46.5$	3.0	2.9	5.3-7.9	1.2-3.2	1.1-3.0	7.0-7.9	-
19691 $53.0 < t < 56.0$	3.0	3.0	4.2-6.5	4.2-6.4	4.6-8.8	-	10.6-17.8
19739 $48.5 < t < 51.5$	3.0	3.0	4.4-5.0	8.2-9.2	4.8-6.8	7.6-8.9	2.6
27578 $44.2 < t < 46.4$	3.3	2.9	6.0-8.0	4.5-6.3	4.6-5.9	10.2-10.6	-
27654 $47.0 < t < 50.0$	4.0	3.4	4.7-6.3	3.2-7.8	3.4 - 5.4	0.4-10.2	-

Together with the dimensionally similar discharge 27658, shot no. 27654 constitutes the core of a ρ^*-scan [3]. The relevant parameters in shot no. 27658 are scaled to $B_t = 1.7$T, $I_p = 2$MA and $P_{RF} = 3.2$MW to provide a larger $\rho^\star$.

In order to assess the performance of the simulations the following profile average [4] was used

$$\frac{\sigma_{T_j}}{T_j} = \frac{\sqrt{\sum_{l=1}^{N}\left(T_{l,j}^{pred} - T_{l,j}^{exp}\right)^2 / N}}{T_j^{max}} \qquad , j = i, e$$

where the sum is over all spatial points. Time averages of these measures are shown below

shot no	averaging interval	$\frac{\sigma_{T_i}}{T_i}$	$\frac{\sigma_{T_e}}{T_e}$	$\frac{\sigma_n}{n}$
15596	$44.0 < t < 46.5$	0.04	0.05	0.10
19691	$53.0 < t < 56.0$	0.09	0.10	0.17
19739	$48.5 < t < 51.5$	0.07	0.11	0.07
27578	$44.2 < t < 46.4$	0.14	0.05	0.12
27654	$47.0 < t < 50.0$	0.08	0.06	0.08

Ion Temperature

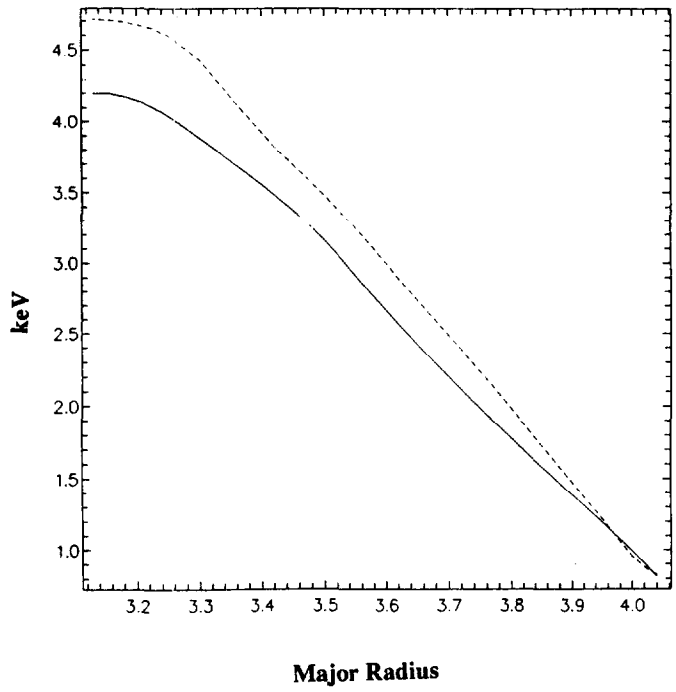

Shot no: 19691

Time: 55.8s(t_{pred} = 2.8s)

Predicted Profiles :————

Experimental Profiles:---------

Electron Temperature

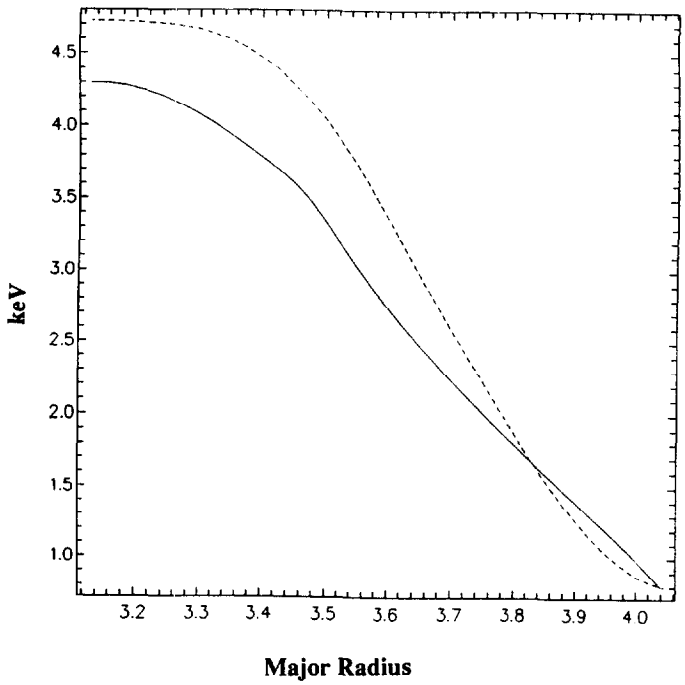

Shot no: 19691

Time: 55.8s(t_{pred} = 2.8s)

Predicted Profiles :————

Experimental Profiles:---------

Density

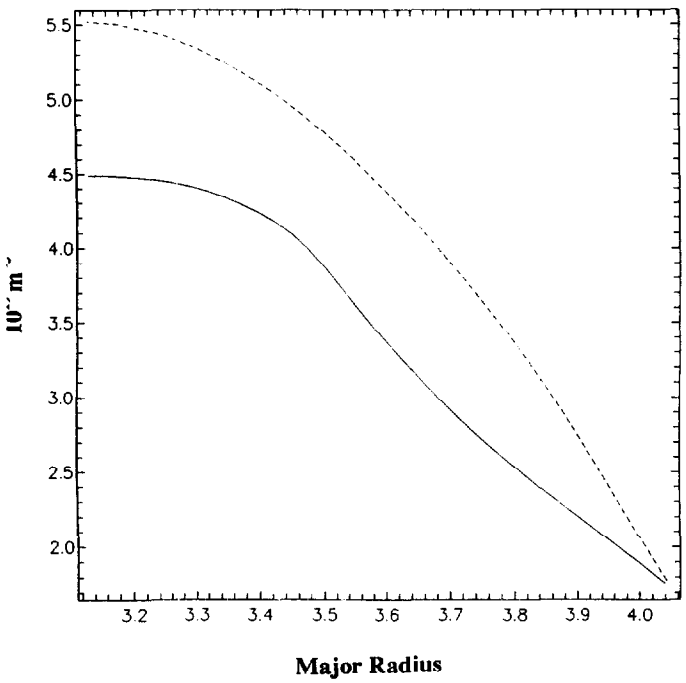

Shot no: 19691

Time: 55.8s(t_{pred} = 2.8s)

Predicted Profiles :————

Experimental Profiles:- - - - - - - -

Effective Ion Heat Conductivity χ_i

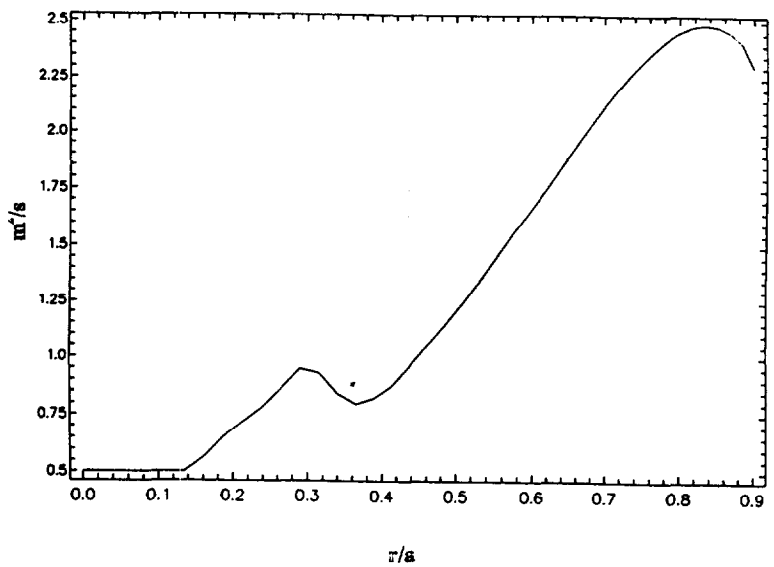

Shot no: 19691

Time: 55.8s(t_{pred}=2.8s)

Relative Errors: Ion Temperature

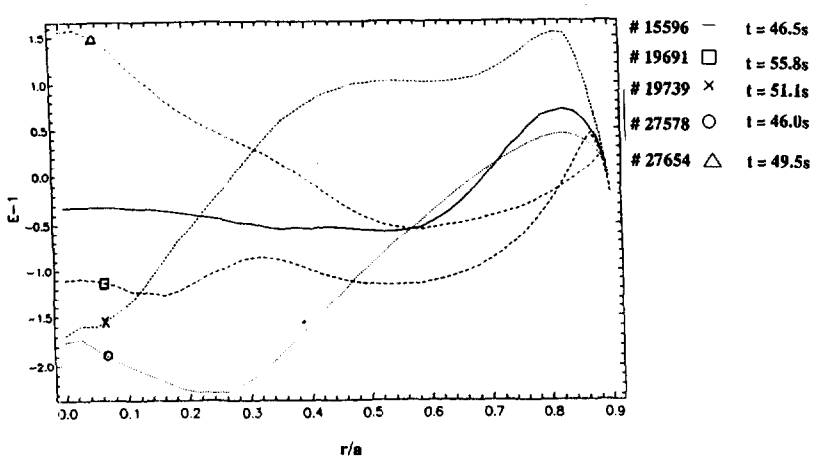

Relative Errors: Electron Temperature

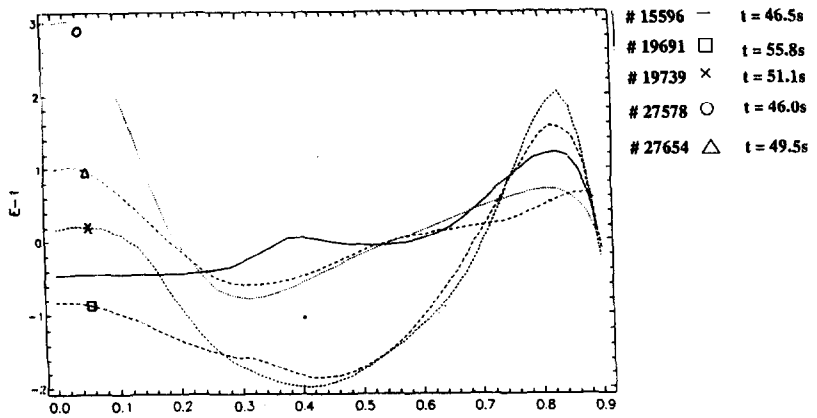

Relative Errors: Density

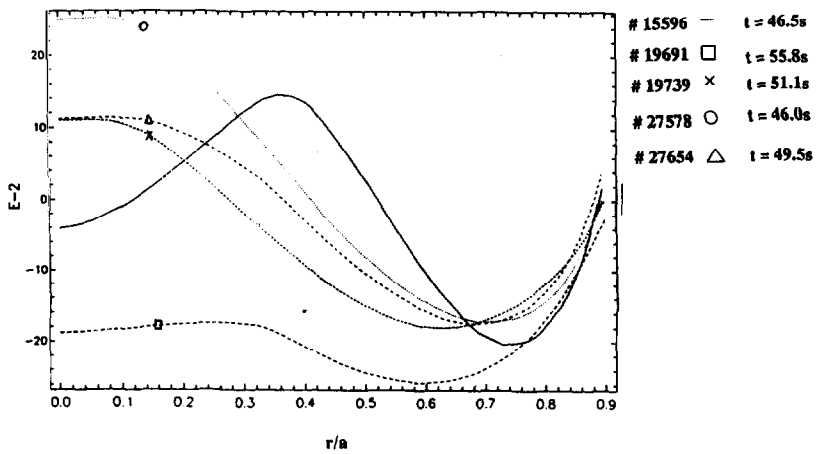

Radial Profiles for # 27654 at t = 51.5s

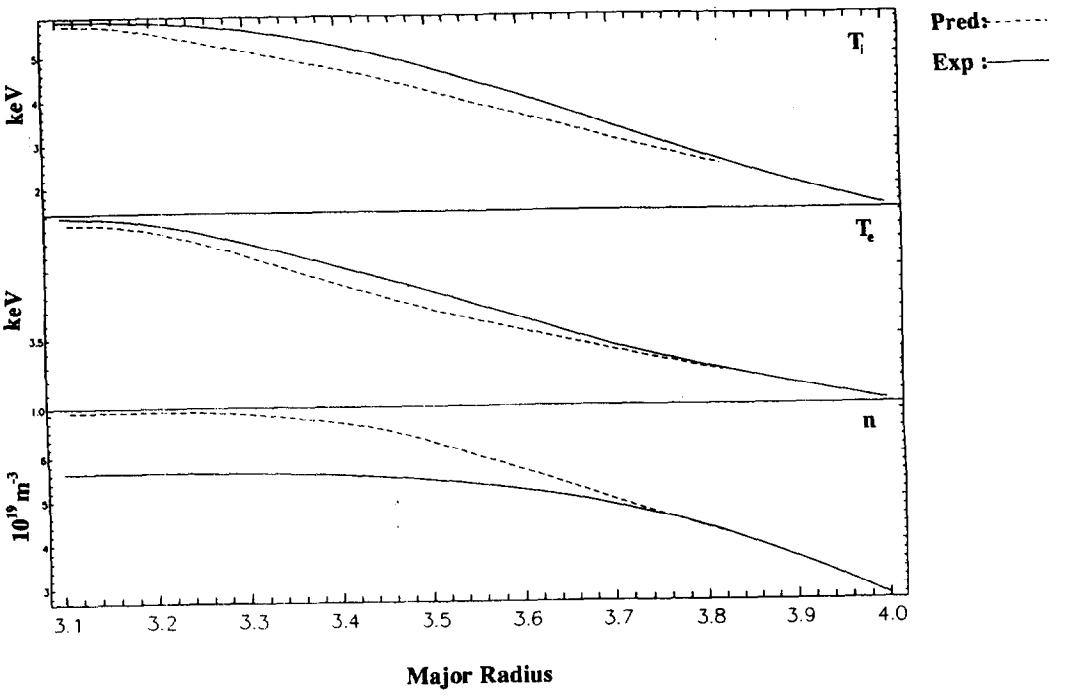

Radial Profiles for #27658 at t = 55.0s

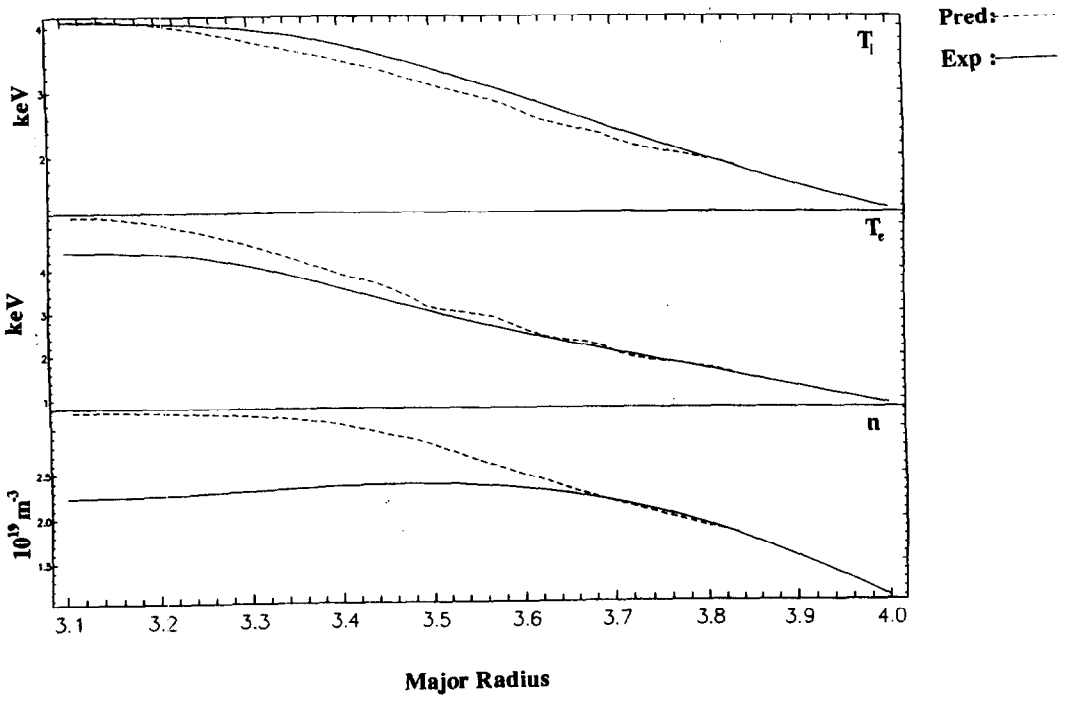

Profile averages: Boundary at r/a = 0.7

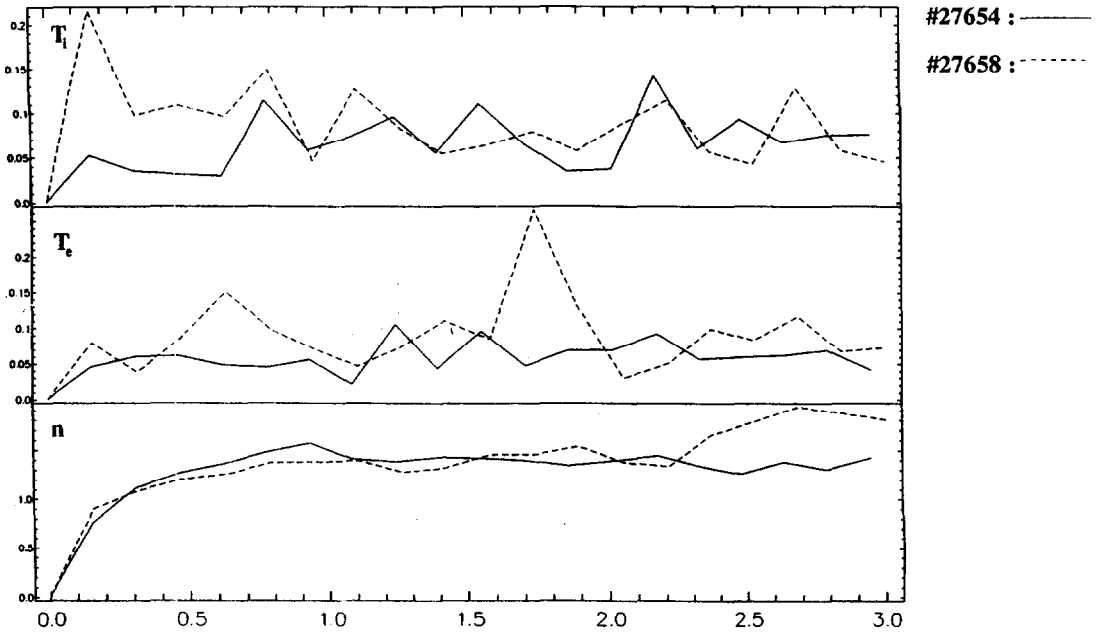

Simulation Time (secs)

Profile averages: Boundary at r/a = 0.9

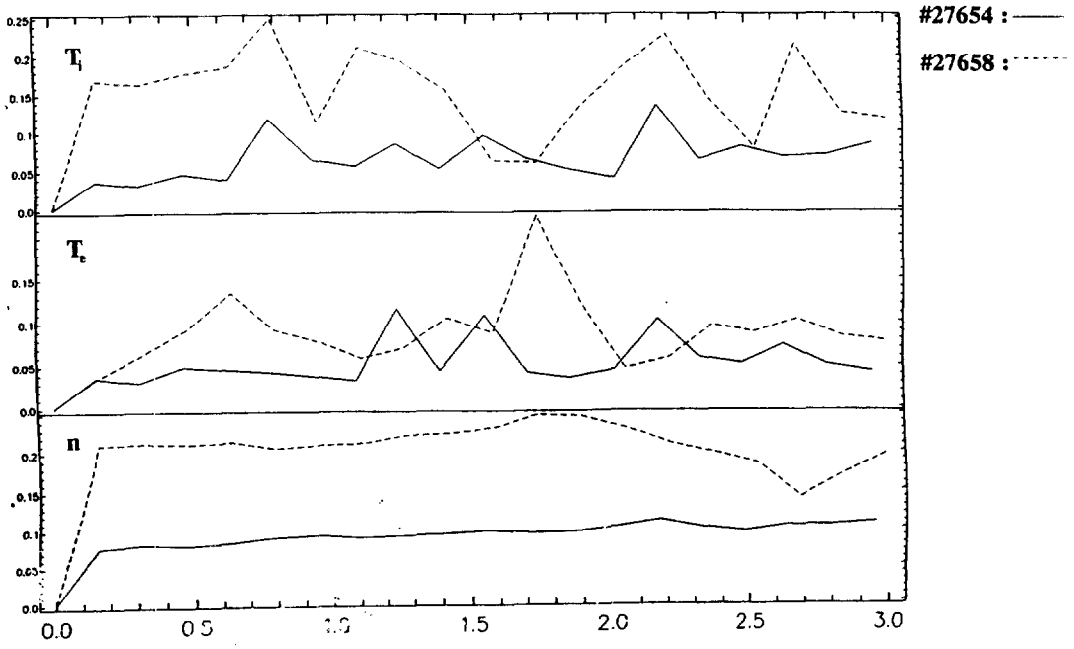

Simulation Time (secs)

Summary

Modelling

- Reactive Drift-wave model intended for the good confinement region (corresponding to $q \approx 1$ and $q \approx 2$). Combines the toroidal branch of the Ion temperature Gradient driven mode (ITG) and the Trapped Electron mode in the collisionless limit (CTE) in one description.
- Conservation relations for energy and density are used to evolve temperature and density profiles together with the transport coefficients in a self-consistent way.
- Initial profiles, source terms and geometrical quantities taken from JET profile databases.

Results

- The predicted profiles were compared with experimental data. In general there was an overestimation of the particle transport with the density tending to the average of n_i and n_e. For the temperature profiles, $T_i(r)$ and $T_e(r)$, relative errors $\leq 20\%$ were achieved whereas the density profiles were reproduced within 25%
- Despite the $T_e^{\frac{3}{2}}$ dependence in the transport coefficients, χ_i^{eff}, χ_e^{eff} and D_e^{eff} show a radial growth out to $r/a \approx 0.8$.
- The comparison in the $\rho^* - scan$ (shots no. 27654, 27658) indicates that these shots are well described by our gyro-Bohm model up to a radius of $r/a \approx 0.8$ whereas the agreement with experiments decreases when the outer boundary is moved towards the edge.

Future Work

- Inclusion of impurities[8] in the comparison. This would probably improve the correlation with experiments by providing a better description of transport by the dynamic introduction of dilution effects.
- A more careful analysis of both L-mode and H-mode $\rho^\star$-scans.
- To include more physics, e.g. finite β effects and $k_{||}$ dynamics.

References

[1] M. Fröjdh, P. Strand, J. Weiland, J.P. Christiansen, CTH-IEFT/PP-1995-07, (1995)

[2] H. Nordman, J. Weiland & A. Jarmén, Nucl.Fusion **30**, 983 (1990)

[3] J.P. Christiansen, P.M. Stubberfield, J.G. Cordey, C. Gormezano, C. Fowers, J. O'Rourke, D. Stork, A. Taroni, Nucl. Fusion **33**, 863 (1993)

[4] G. Bateman, Phys. Fluids **B4**, 634 (1992)

[5] G. Cenacchi & A. Taroni, JET-IR(88) 03

[6] J. Blum & J.Le Foll, J. Comput. Phys., Rep 1, 465 (1984)

[7] R.J. Goldston, D.C. McCune, H.H. Towner, S.L.Davis, R.J. Hawryluk & G.L. Schmidt, J. Comput. Phys., **43**, 61 (1981)

[8] G. Bateman, J. Weiland & H.G. Gustavsson, Bull. Am. Phys. Soc. **38**, 2038, Paper 6T17 (1993)

Movement of the Radiative Zone from Target to X-Point in Radiative Divertor Scenarios

R A M Van der Linden, G T A Huysmans, W Kerner, R Reichle, J A Wesson.
JET Joint Undertaking, Abingdon, Oxfordshire, OX14 3EA, UK.

ABSTRACT

In radiative divertor experiments, the radiative zone is observed to move away from the target plates to the X-point region as the plasma detaches. In this paper, straightforward model calculations for this phenomenon are presented. Solving a simplified one-dimensional energy balance equation, taking specifically the presence of a magnetic X-point into account, it is shown that the fast movement of the radiative zone to the X-point region is a natural consequence of the increase in global radiation levels.

INTRODUCTION & MOTIVATION

The preferred solution to the ITER power exhaust problem is to use a deep, closed divertor to

- radiate away a significant fraction of the exhaust power to reduce target load
- prevent bulk plasma contamination by (eroded) impurities

A common feature of tokamak divertor experiments is that as the plasma detaches from the divertor plates, the zone that radiates most energy ('radiative zone') moves away from the target plates to the X-point region on a short time-scale, and then remains there as total radiation power is further increased. The radiation in the divertor region itself drops to virtually zero. At some critical total radiation level the radiative zone moves further up (and inside the separatrix), which rapidly results in a density limit disruption. Qualitatively similar behaviour is observed in detailed numerical modelling of divertor plasmas.

Does the radiative zone move from target to X-point due to a (radiative) instability or is it a continuous movement ? There seems to be no general consensus yet [1] [2] [3].

In the following we first present a simple physics model based on the balance between radiation and effective conduction, outlining the fundamental ingredients responsible for the rapid movement of the radiative zone. It is shown that a global increase in the radiation level (due to an increase in either density or impurity fraction) results in a *continuous* movement of the radiative zone from target to X-point. Once the radiative zone has started to move, small changes in density lead to substantial movements.

There is relatively good qualitative agreement with JET experimental results. As in the model the movement of the radiative zone in JET is clearly continuous; the radiative zone does not 'jump' to the X-point, but gradually moves there in response to changes in the plasma properties (density or impurity levels). This movement seems to be inevitable if good (complete) detachment is to be obtained (at least with the present divertor configuration). In spite of the fairly narrow operational window between detachment and the density limit [4], experiments in JET have established that a detached plasma with X-point radiation can be succesfully maintained and a density limit disruption avoided.

A SIMPLE PHYSICS MODEL

To describe the essential ingredients responsible for the radiative zone movement, consider the energy balance equation for $\mathbf{v} = 0$ and $\kappa_\perp = 0$ ($\rightarrow$ source term).

$$\rho C_v \frac{\partial T}{\partial t} = \nabla \cdot \left[\kappa_{\parallel} (\mathbf{B} \cdot \nabla T) \mathbf{B} / B^2 \right] - L + H \,, \qquad (1)$$

where the first term in the right hand side represents thermal conduction along the field lines, L is the radiation, and H the energy source term.

In equilibrium with $B \approx B_{tor} \approx const$, T= axisymmetrical, this becomes

$$\frac{B_{pol}}{B} \frac{\partial}{\partial l_p} \left(\kappa_{\parallel} \frac{B_{pol}}{B} \frac{\partial T}{\partial l_p} \right) - L + H = 0 \,, \qquad (2)$$

where l_p is the distance along a poloidal cross-section of a flux surface. Since

$$B_{pol}(X\text{-point}) << B_{pol}(\text{target}),\ B_{pol}(\text{midplane})$$

the X-point region acts as a *'temperature barrier'* with strongly reduced conduction in the poloidal coordinate.

MODEL INGREDIENTS

We use JET-relevant parameters:

- **Total poloidal distance**:

$$L_p \approx 8m,\ l_p^* = l_p/L_p$$

- **Poloidal Field:** replace the typical experimental profile with a symmetric model profile

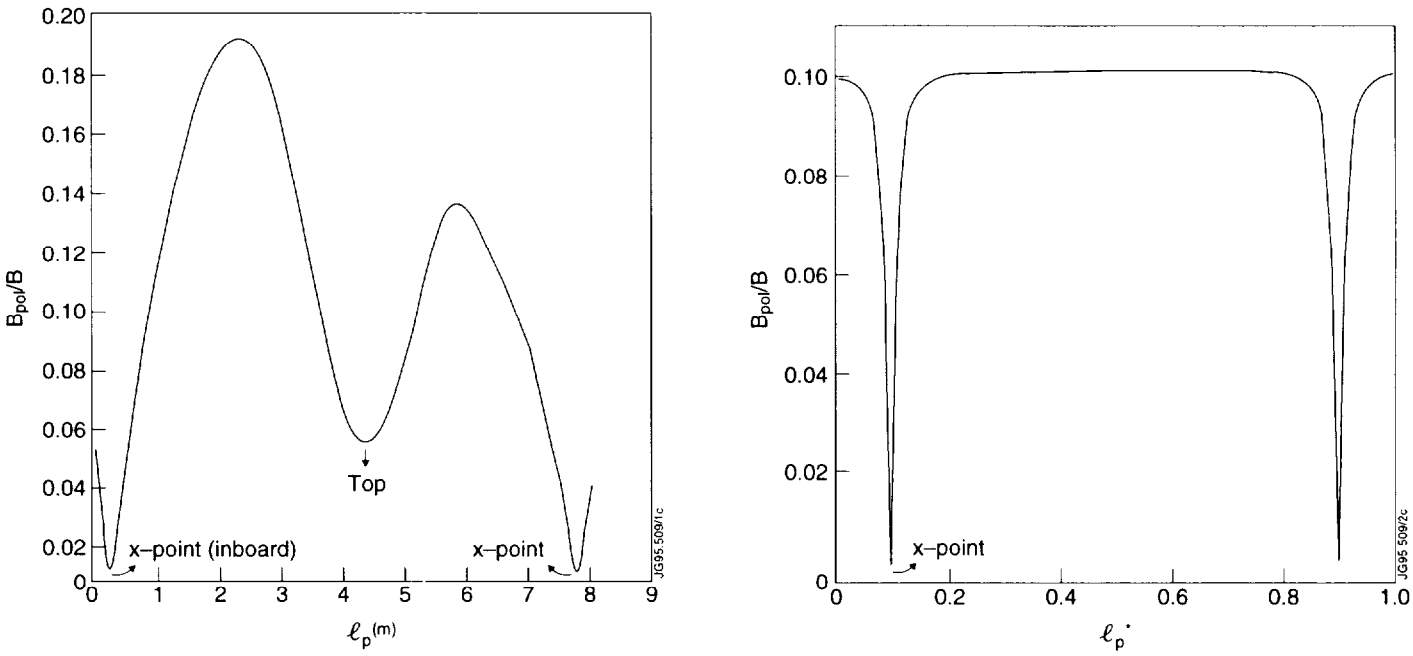

Figure 1a) A typical experimental profile for the poloidal magnetic field close to the separatrix; b) the model profile of the poloidal field used in the calculations.

- **Heating Source Term**: take a constant heat source per unit volume in the upstream region, but switch off the heating term at $l_p = l_{p,H}$, a short distance *above* the X-point.

Typical value: $H_0 = 1.7 MW/m^3$.

- **Conduction:** use classical parallel conduction coefficient: $\kappa_{\parallel} = 10^{-11} T^{5/2} W m^{-1} K^{-1}$. Scaling temperature to $T_c = 10^6\ K \approx 100 eV$ yields a dimensionless ratio

$$\frac{H_0 L_p^2}{10^{-11} T_c^{7/2}} \approx 0.01.$$

- **Boundary Conditions:** in the calculations reported here we keep $T(0) = T(l_p)$ fixed at a low value. An alternative is to use 'sheath boundary conditions' by specifying that the energy conducted to the target plasma sheath is equal to the energy carried away (to the target) by

Mach-1 parallel flow. This leads to a boundary condition relating temperature to the temperature gradient:

$$\kappa_{\parallel} \frac{\partial T}{\partial l_p} = \pm c T^{3/2}$$

- **Radiation**: model radiation function with assumptions about density or pressure:

$$L = \rho \mathcal{L}(T) \propto \frac{p\mathcal{L}}{T}$$

→ assume p or ρ constant along l_p and increase radiation amplitude.

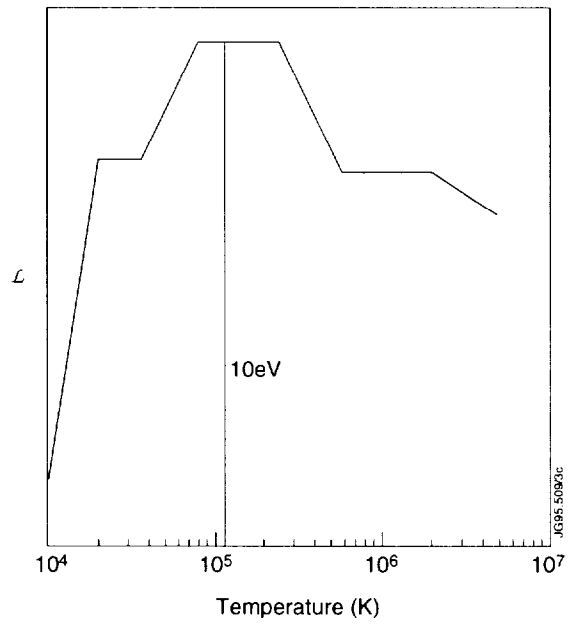

Figure 2. The model radiation function $\mathcal{L}$ as a function of temperature

MODEL RESULTS

Equation (1) is solved using linear finite elements and an implicit time-stepping algorithm taken from the SOL-ONE code [5]. Typical equilibrium temperature profiles are displayed in figure 3. The effect of the reduced conduction near the X-point is obvious.

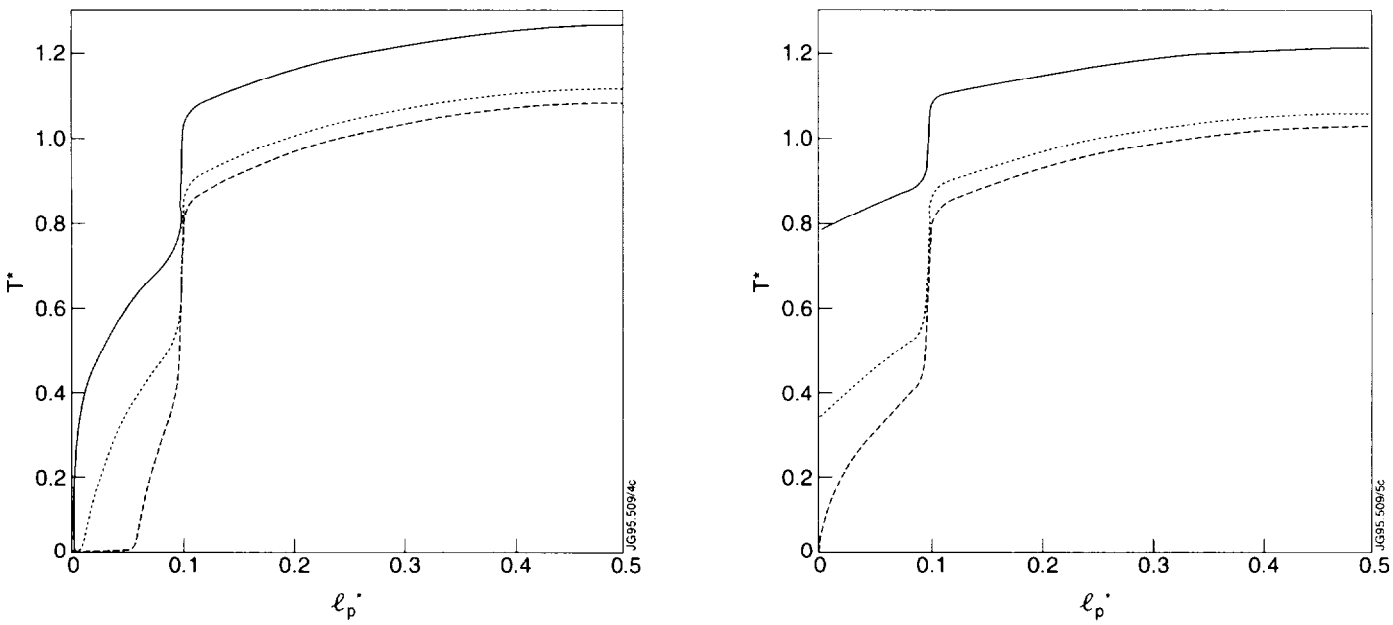

Figure 3. Typical temperature profiles for low to moderate radiation levels, using fixed temperature boundary conditions (left) and 'sheath' boundary conditions (right).

By gradually increasing the amplitude of the radiation fucntion we mimic the effect of an increase in impurity concentration or density, in line with usual experimental procedures. We then calculate how the temperature profile and the radiation distribution respond to the global increase in radiation. The results for a typical case are shown in figures 4, 5, 6.

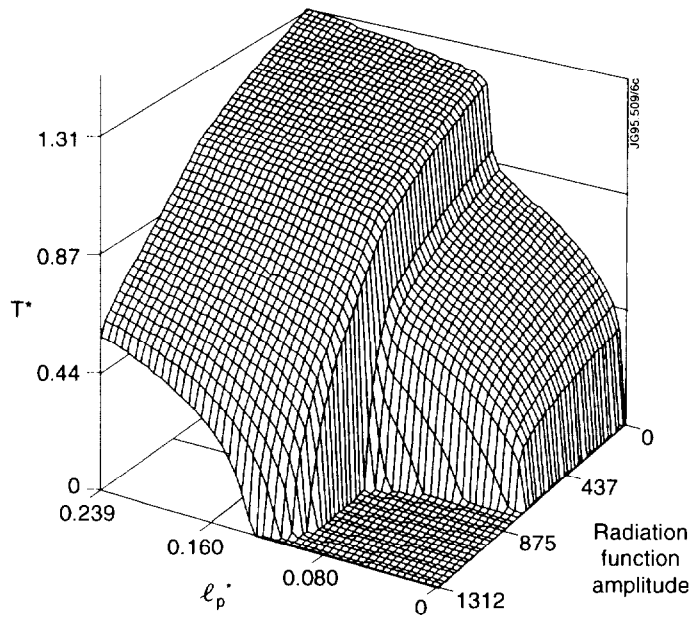

Figure 4. Temperature profiles for increasing global radiation values.

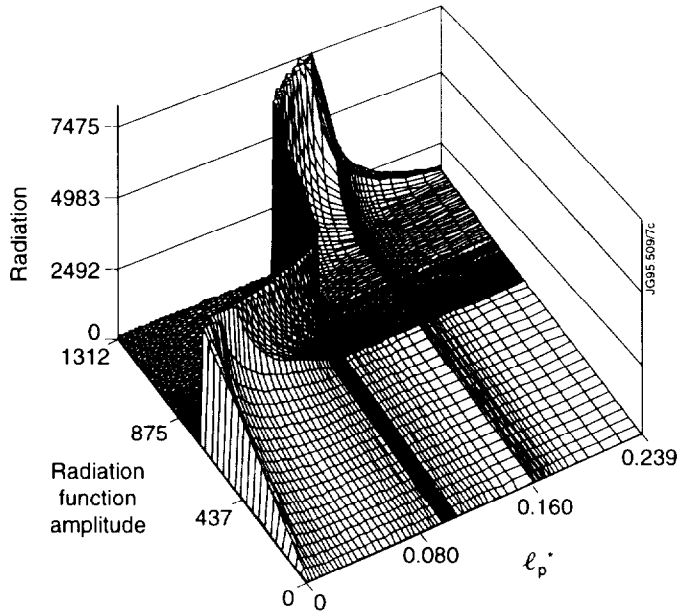

Figure 5. Radiation distribution in the poloidal coordinate for increasing global radiation values.

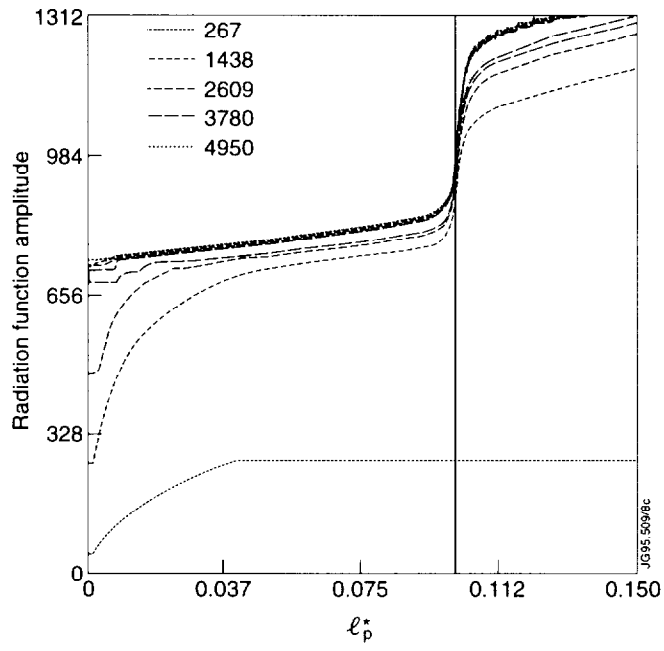

Figure 6. Contour plots of the radiation distribution for increasing global radiation.

The results shown above are typical and lead to the following conclusions:

- Increasing the global level of radiation first leads to increased radiation predominantly near the target plates.
- Beyond a critical radiation level there is a 'fast' (i.e. over a narrow range in density or impurity concentration) movement of the radiative zone from target to X-point as the discharge moves to detachment.
- After that, the radiative zone 'sticks' to the X-point region.
- There is *no instability*: in this model we obtained a *continuous transition from target radiation to X-point radiation.*

JET EXPERIMENTAL RESULTS

For comparison with experimental results (see Reichle et al. [1] for a more detailed description of the radiation distribution) we first look at a typical discharge with intrinsic impurities only (.i.e. the radiation is carbon-dominated). Figure 7 shows the radiation as measured by bolometers at different heights in the divertor region (height increases from a to d). It is clear from this graph that as the density (and thus the radiation level) is increased, the radiation near the target plates peaks and then decreases monotonically. After that the maximum radiation is reached at subsequently higher positions.

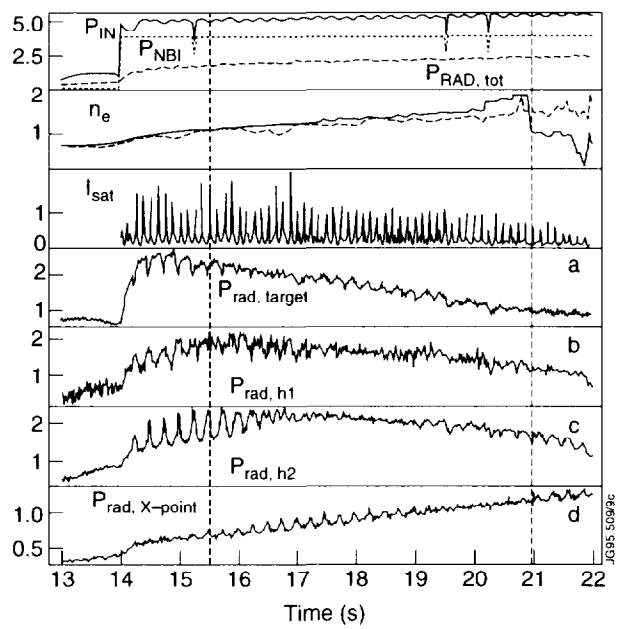

Figure 7. Overview of discharge 31504. The lower four traces are bolometer measurements at distances from the target increasing from a to d.

The discharge shown ended in a density limit disruption. However, using a feedback on the nitrogen content, it has been demonstrated in JET that a detached radiative divertor discharge with dominant X-point radiation can be maintained and terminated without a disruption. An example of such a discharge is shown in figure 8. Again, the movement of the radiative zone to the X-point is obvious. Then, the zone stays near the X-point during the detached phase of the discharge, until the nitrogen input is switched off.

CONCLUSIONS

- The observed movement of the radiative zone from target to X-point can be ascribed to the global increase of radiation levels due to e.g. higher densities or impurity concentrations.
- Both the simple 1D model and the experimental results obtained in JET point to a *continuous (stable)* movement of the radiative zone rather than a response to an instability.
- There is a relatively small operational window between detachment (when the radiative zone starts to move) and dominant X-point radiation.
- The radiative zone 'sticks' near the X-point due to the B_{pol} 'barrier' and (detached) discharges with dominant X-point radiation can be succesfully concluded without disruption.

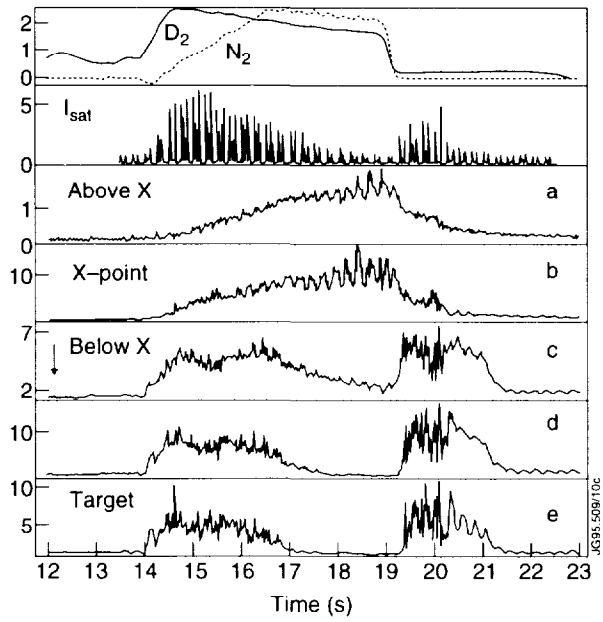

Figure 8. Overview of discharge 33192. The lowest 5 traces are radiation measured at increasing heights (from a to e).

REFERENCES

[1] R. Reichle et al. Proc. 22nd EPS Conf., Bournemouth, UK (1995).

[2] J.C. Fuchs et al. Contrib. 21st EPS Conf., Montpellier, France (1994).

[3] T.P. Petrie et al. J. Nucl. Mater. 196-198, 848 (1992).

[4] I.H. Hutchinson, Nuclear Fusion **34**, 1337 (1994).

[5] G.T.A. Huysmans and K. Borrass, JET Report, to be published.